

**Magnetic, electronic, and thermal properties of buckled kagome  $\text{Fe}_3\text{Ge}_2\text{Sb}$** Quinn D. Gibson,<sup>1</sup> Ramzy Daou,<sup>2</sup> Marco Zanella,<sup>1</sup> Jonathan Alaria,<sup>3</sup> and Matthew J. Rosseinsky<sup>1</sup><sup>1</sup>*Department of Chemistry, University of Liverpool, L69 7ZD, United Kingdom*<sup>2</sup>*Department of Physics, Normandie Univ, ENSICAEN, UNICAEN, CNRS, CRISMAT, 14050 Caen, France*<sup>3</sup>*Department of Physics, University of Liverpool, L69 7ZE, United Kingdom*

(Received 23 February 2023; revised 11 May 2023; accepted 18 May 2023; published 5 July 2023)

The magnetic, electronic, and thermal properties of  $\text{Fe}_3\text{Ge}_2\text{Sb}$  single crystals, a derivative of the hexagonal FeGe structure with a buckled Fe kagome net and Sb-Sb dimers are reported. Electronic structure calculations show most of the kagome-derived bands remain intact with the Fe buckling, with the exception of a van Hove singularity near the Fermi level, which is selectively destroyed. This selective destruction of the van Hove singularity is associated with the lack of a charge order transition in  $\text{Fe}_3\text{Ge}_2\text{Sb}$  compared to FeGe. Magnetization measurements show two antiferromagnetic transition at 290 K and 16 K. The low-temperature transition is attributed to spin canting and is associated with a metamagnetic transition observed in the isothermal magnetization below the transition temperature. Electrical and thermal transport measurements show metallic behavior, and more significant magnetic scattering associated with the metamagnetic transition is observed in the magnetothermal conductivity compared to the magnetoresistance. This is consistent with a modification of the long-period magnetic structure that modifies preferentially small angle scattering thus having a strong impact on thermal transport properties. We conclude that buckled  $\text{Fe}_3\text{Ge}_2\text{Sb}$  exhibits similar properties to unbuckled hexagonal FeGe with the exception of the lack of a charge density wave transition in  $\text{Fe}_3\text{Ge}_2\text{Sb}$ , likely due to the selective destruction of the van Hove singularity near  $E_F$ , making the family of compounds  $\text{Fe}_3\text{Ge}_{3-x}\text{Sb}_x$  a good host to study various physical effects in kagome metals, especially the electronic and structural stabilization of charge ordered states.

DOI: [10.1103/PhysRevB.108.035102](https://doi.org/10.1103/PhysRevB.108.035102)**I. INTRODUCTION**

The kagome net is a geometric feature of vertex sharing triangles that lie in a plane. Kagome metals are a class of materials wherein a set of atoms of a single type are arranged in this geometry. In theory, the magnetic or electronic Hamiltonian that arises from this geometry should lead to unconventional magnetic or electronic ground states, such as frustrated magnetism and possible spin-liquid phases resulting from magnetic interactions on the kagome net [1–3], and flat bands and Dirac cones resulting from electronic orbital interactions [4,5]. Kagome metals, or materials that have delocalized electrons that stem from the orbital interactions of the kagome net, have been of recent interest due to a variety of complex electronic and magnetic phenomena, such as superconductivity, chiral charge density waves (CDW) with an accompanying chiral transport effect and unconventional anomalous Hall effect in the  $\text{AV}_3\text{Sb}_5$  ( $A = \text{K}, \text{Rb}, \text{Cs}$ ) family of materials [6–10], coexistence of massive Dirac fermions and noncolinear ferromagnetism in  $\text{Fe}_3\text{Sn}_2$  [11,12], and Weyl states and a zero field Nernst response in  $\text{Co}_3\text{Sn}_2\text{S}_2$  [13,14].

In some of these real kagome materials, the ideal two-dimensional (2D) kagome geometry is perturbed by atoms

that bridge the kagome layers in the third direction. The hexagonal FeGe structure (referred to in the ICSD as the CoSn structure type, as it shares a structure with CoSn and FeSn, and is distinct from the cubic FeGe structure) exists at the 2D end of the  $\text{A}_3\text{X}-\text{A}_3\text{X}_2-\text{AX}$  kagome materials family where  $A$  is the transition metal and  $X$  is a main group element. In FeGe, all of the transition metal is confined to kagome planes, separated by layers of Ge. As such, it is considered a good kagome metal and has been reported to host the resulting Dirac fermions and flat bands in its electronic structure in magnetic FeSn [15] and orbital selective Dirac bands and flat bands in nonmagnetic CoSn [16–18]; the presence of these electronic features is considered most robust when there is no transition metal bridging the kagome layers [19]. FeGe itself also has been shown to demonstrate charge order, similar to that in the  $\text{AV}_3\text{Sb}_5$  family [20,21], which has been shown to be stabilized by a van Hove singularity near the Fermi level [22]. There also exists a stuffed variant of the FeGe structure, which can be written as  $\text{A}(\text{V}, \text{Cr}, \text{Mn}, \text{Fe}, \text{Co})_6(\text{Sn}, \text{Ge})_6$  [23], and has shown to host a variety of novel properties, such as quantum limit Chern magnetism in  $\text{TbMn}_6\text{Sn}_6$  [24], large anomalous Hall effect in  $\text{LiMn}_6\text{Sn}_6$  [25], and nontrivial band topology in  $\text{YV}_6\text{Sn}_6$  [26]. The  $\text{AV}_3\text{Sb}_5$  family can also be considered as an alkali and main group intercalated version of the FeGe structure type, putting it closer to the 2D kagome limit. Overall, an understanding of the interaction between the transition-metal kagome net as well and the connecting p-block elements as well as the stuffed atoms is key to understanding the variety of properties in this structural family. The charge order in FeGe

Published by the American Physical Society under the terms of the [Creative Commons Attribution 4.0 International](https://creativecommons.org/licenses/by/4.0/) license. Further distribution of this work must maintain attribution to the author(s) and the published article's title, journal citation, and DOI.

and the  $AV_3Sb_5$  family are of particular interest, modifying the structure and thus the electronic structure, particularly the van Hove singularities as present in FeGe and  $AV_3Sb_5$ , can further understanding of the microscopic origin of the charge order.

Here we report on the magnetic and transport properties of  $Fe_3Ge_2Sb$  single crystals, a ternary variant of the FeGe structure type with an expanded cell and a buckled kagome net due to Sb-Sb dimerization, previously reported in Ref. [27]. We compare the calculated electronic structure of the unbuckled FeGe structure with that of  $Fe_3Ge_2Sb$  in the antiferromagnetic state showing the presence of kagome-derived Dirac bands below the Fermi level in both FeGe and  $Fe_3Ge_2Sb$  and the selective destruction of a van Hove singularity near the Fermi level. Further, no charge order transition is observed, supporting the finding that the kagome derived van Hove singularity near  $E_F$  plays an important role in stabilizing the charge order [22], and that even a small amount of buckling removes this feature. Magnetic measurements demonstrate a transition into an antiferromagnetic state at 288 K, followed by a canted spin state below 16 K. This canted spin state has a metamagnetic transition near 2 T at 2 K. The magnetic scattering associated with the metamagnetic transition has a much larger effect on the scattering of phonons than electrons, consistent with the interpretation of it as a long-period field-induced modification of the magnetic structure. While we observe no features stemming from the Dirac state in the transport measurements (likely because it is below the Fermi level), the weak coupling of the electronic properties to the spin-canting modification indicates that the calculated electronic states of  $Fe_3Ge_2Sb$  are likely retained in the canted state, indicating that the electronic structure may be robust to the precise magnetic structure in this materials family.

## II. MATERIALS AND METHODS

$Fe_3Ge_2Sb$  crystals were grown by annealing a stoichiometric sample in an evacuated quartz ampoule at 973 K for two weeks. Fe chunk, Ge chunk, and Sb pieces were weighed out in stoichiometric quantities and placed in a quartz ampoule that was subsequently evacuated. This sample was heated to 973 K for 12 h, followed by a grinding of the resulting mixture, resealing in an evacuated quartz tube and reheating at 973 K for two weeks. Small, chunky hexagonal crystals (about  $1\text{ mm}^3$ ) were isolated from the resultant mixture, coexisting with rodlike single crystals of  $Fe_{1.67}Ge$ . The structure and composition of the crystals was confirmed by single crystal x-ray diffraction. The structure was further confirmed by performing powder x-ray diffraction on crushed crystals.

A suitable crystal was selected and measured on a dtrek-CrysAlisPro-abstract goniometer imported rigaku-dtrek images diffractometer. The crystal was kept at 100 K during data collection. Small pieces of the chunky hexagonal crystals were removed via scalpel for measurement. Data had an  $R_{\text{int}}$  of 4.04% with a resolution to  $0.70\text{ \AA}$  and an  $\frac{I}{\sigma}$  of 50.9. The crystal structure refinement was performed in Olex2 [28] using ShelXT structure solution program [29] using Intrinsic Phasing and refined with the ShelXL [30] refinement package using least squares minimization. The final structural model had an  $R_1 = 2.33\%$ ,  $wR_2 = 5.06\%$  and a goodness of fit

TABLE I. Refined atomic position and occupancy parameters for  $Fe_3Ge_{2.085(4)}Sb_{0.915(4)}$ .

Label	Atom	x	y	z	occ
Sb1	Sb	0	0	0.82188(13)	1
Sb2	Sb	2/3	1/3	0.6794(2)	0.831(7)
Ge1	Ge	0.68459(9)	0.68459(9)	0.5	1
Ge2	Ge	0.65285(9)	0.65825(9)	1	1
Fe1	Fe	0.83267(5)	0.66533(11)	0.75512(9)	1
Fe2	Fe	0.5	0.5	0.74051(14)	1
Ge3	Ge	2/3	1/3	0.744(2)	0.179(7)

of 1.139. The space group was determined to be  $P6/mmm$  with unit cell parameters  $a = 8.9070(5)\text{ \AA}$  and  $c = 7.9217(7)\text{ \AA}$ . The refined atomic positions and occupancies are reported in Table I. The lattice parameters and atomic positions agree with those reported in Ref. [27], with some small deviations in refined occupancies as discussed in Sec. III. Laboratory powder x-ray diffraction data were collected on a Bruker D8 Advance diffractometer in Debye-Scherrer geometry using monochromated Cu  $K_{\alpha 1}$  incident radiation with a scanning position sensitive detector. Samples were prepared as thin foils and were supported on a rotating sample stage during the measurement. Powder x-ray diffraction pattern of crushed crystals was fit well to the  $Fe_3Ge_2Sb$  structure, with a small impurity of  $Fe_{1.67}Ge$ ; these can generally be separated from the crystals of  $Fe_3Ge_2Sb$  due to the rodlike morphology of  $Fe_{1.67}Ge$  compared to the chunk and platelike morphology of  $Fe_3Ge_2Sb$ .

Scanning electron microscopy (SEM) and energy dispersive x-ray spectroscopy (EDX) was performed with a Hitachi S4800 equipped with an EDX detector from Oxford Instruments. Samples were deposited on a carbon tape attached on an aluminium stub and coated with a thin film of carbon before performing imaging and EDX. Chemical quantification was performed using INCA software from Oxford Instruments.

Magnetic properties were measured on  $Fe_3Ge_2Sb$  single crystals glued on a quartz paddle using a Quantum Design Magnetic Properties Measurement System using vibrating sample magnetometry. Crystals were aligned along particular crystallographic directions using the natural facets of the crystal. The  $c$  axis was determined by the presence of a hexagonal facet and was confirmed by the temperature dependence of the magnetization versus temperature measurement via an absence of a low-temperature minimum as present in the  $ab$  plane of FeGe [31].

Heat capacity was measured on a 1.3 mg single crystal of  $Fe_3Ge_2Sb$  using Quantum Design Physical Properties Measurement System (PPMS) using the relaxation method. Heat capacity at from 1.8–250 K was measured using low-temperature N grease. Due to the typical crystal mass (about 1 mg), reliable heat capacity data was not achieved above 220 K; however, a heat capacity anomaly is expected around 290 K due to the antiferromagnetic transition. Heat capacity was modeled as a linear combination of Debye and Einstein terms and a linear electronic  $\gamma$  term as shown in Eq. (1).

$$C_P(T) = a_1 C_D(T, \theta_{D1}) + a_2 C_D(T, \theta_{D2}) + a_3 C_E(T, \theta_E) + \gamma T, \quad (1)$$

where the sum of  $a_1$ ,  $a_2$  and  $a_3$  was constrained to be 1, and  $C_D(T)$  and  $C_E(T)$  represent the Debye and Einstein expressions for the heat capacity, respectively [32].

Electrical contacts were made to a small single crystal of dimension  $0.7 \times 0.4 \times 0.04 \text{ mm}^3$  using Dupont 4929 silver paint and  $50 \text{ }\mu\text{m}$  silver wires. Contact resistances were around  $1 \text{ }\Omega$ .

Electrical resistivity and Hall effect were measured on the single crystal in the PPMS cryostat using a standard four-probe technique employing an alternating current source and lock-in amplifier. Currents up to  $1 \text{ mA}$  were used with no detectable heating.

Thermal and thermoelectric transport were measured on the same single crystal using the standard one-heater, two-thermometer technique on a custom built PPMS puck with custom electronics and software. Temperatures were measured using Cernox chip resistors and thermoelectric voltages were recovered using an A10 nanovolt preamplifier (EM Electronics) coupled to a Keithley multimeter. At temperatures above  $100\text{K}$  type-E thermocouples were used for thermometry in conjunction with a calibrated heat pipe [33] to determine the heat flowing through the sample in order to compensate for radiation losses.

Electronic structure calculations were performed using the WIEN2K package [34]. For FeGe, a 2000 point  $k$  mesh was used, while for  $\text{Fe}_3\text{Ge}_2\text{Sb}$  a 1000 point  $k$  mesh was used due to the larger unit cell and corresponding smaller Brillouin zone. Experimental lattice parameters and atomic positions were used for the calculations. For the purposes of calculation, a perfectly ordered version of the structure of  $\text{Fe}_3\text{Ge}_2\text{Sb}$  was used. For both calculations, the Perdew-Burke-Ernzerhof functional [35] was used as the exchange functional. Spin-polarized calculation was performed, for FeGe in a  $1 \times 1 \times 2$  supercell geometry, with the initial magnetic structure built to reflect the colinear antiferromagnetic state. Due to the doubling of the  $c$  axis in  $\text{Fe}_3\text{Ge}_2\text{Sb}$ , no supercell was needed for the colinear antiferromagnetic state. The final converged solution for both materials retained this magnetic structure to within error. Spin orbit coupling was included as a perturbative step. Electronic structures were plotted using the W2KPLOTT PYTHON package.

### III. RESULTS AND DISCUSSION

#### A. Crystal structure

The structure of  $\text{Fe}_3\text{Ge}_2\text{Sb}$  was confirmed by single-crystal x-ray diffraction to be the same structure as reported in Ref. [27].  $\text{Fe}_3\text{Ge}_2\text{Sb}$  is isostructural to  $\text{Co}_3\text{Ge}_2\text{Sb}$  [36], which crystallizes in a superstructure of the hexagonal FeGe crystal structure (which can also be written as  $\text{Fe}_3\text{Ge}_3$ ). In FeGe, a  $\text{Fe}_3\text{Ge}$  layers with a kagome ordering of Fe kagome layer is separated by a hexagonal  $\text{Ge}_2$  layer [Fig. 1(a)]. In  $\text{Fe}_3\text{Ge}_2\text{Sb}$ , the Sb preferentially substitutes for the Ge atom in the  $\text{Fe}_3\text{Ge}$  layer [Fig. 1(b)]. These Sb atoms displace along  $c$ , forming dimers that alternate between the layer above and below, leading to a  $\sqrt{3} \times \sqrt{3} \times 2$  expansion of the unit cell and a retention of the  $P6/mmm$  symmetry along with a  $30^\circ$  rotation of the cell axis. The extra charge from Sb is compensated for by the formation of Sb-Sb dimers, which in turn cause a buckling effect in the  $\text{Fe}_3\text{Sb}$  kagome layer. Indeed, this

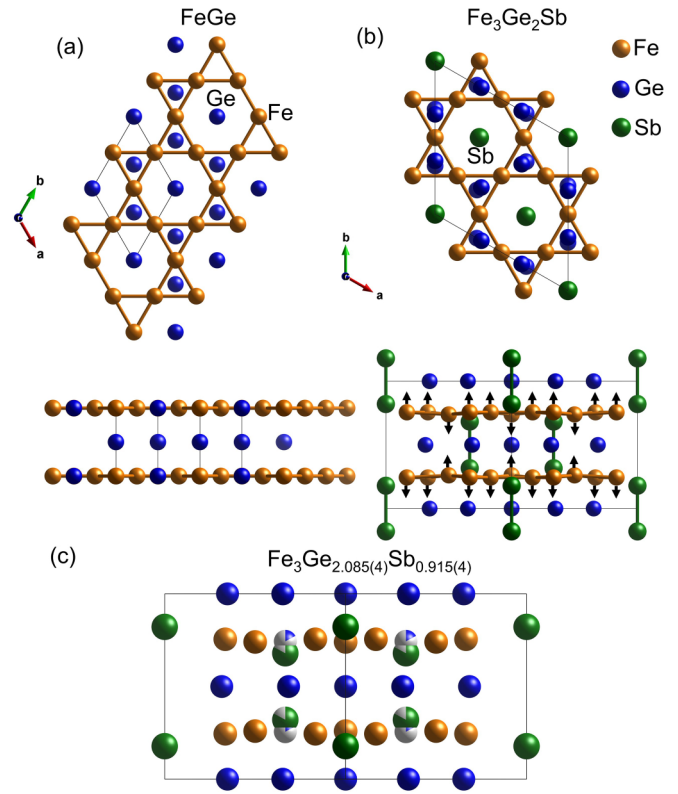


FIG. 1. (a) Structure of FeGe shown from a top-down view (top) and side view (bottom). (b) Structure of  $\text{Fe}_3\text{Ge}_2\text{Sb}$  shown from a top-down view (top) and a side view (bottom). The crystallographic axes have been rotated for ease of structural comparison between the two. Fe-Fe bonds are shown in both panels to highlight the kagome network. Sb-Sb bonds are shown for  $\text{Fe}_3\text{Ge}_2\text{Sb}$  to highlight the dimerization effect. Arrows are shown on the Fe atoms to highlight the displacement from the kagome position of the Fe, demonstrating the buckling effect. (c) The refined experimental structure with refined composition of  $\text{Fe}_3\text{Ge}_{2.085(4)}\text{Sb}_{0.915(4)}$ , showing the 17.9(7) percent Ge for Sb substitution at every other Sb site (the Sb2 site), and the preference for the Ge to sit within the Fe kagome layer.

same dimerization effect is suggested at low temperature in the charge density wave phase of FeGe [37] due to coupling of a van Hove singularity with a soft phonon mode; the presence of Sb appears to stabilize this structural distortion to high temperatures. The buckling effect also splits the kagome Fe layers into two chemically distinct hexagonal sublattices, depending if the Fe is displaced upwards or downwards. A side by side comparison of the room temperature FeGe and  $\text{Fe}_3\text{Ge}_2\text{Sb}$  structures are shown in Fig. 1. Ordered ternary variants also exist with isoelectronic substitutions, e.g., in the  $\text{Co}_3\text{Sn}_{3-x}\text{Ge}_x$  phase field [38].

In the original report of the structure of  $\text{Fe}_3\text{Ge}_2\text{Sb}$ , a 10% vacancy was refined for the Sb site, leading to a true formula of  $\text{Fe}_3\text{Ge}_2\text{Sb}_{0.9}$  [27]. In our crystal structure solution, we confirmed an occupancy of 0.831(7) for one of the two Sb sites (labeled Sb2 in refined atomic positions and occupancies in Table I). However, we also found that this vacancy was compensated for by excess electron density in the center of the kagome layer (where the Ge atom sits in FeGe) below the Sb2 site, labeled the Ge3 site. If the electron density is

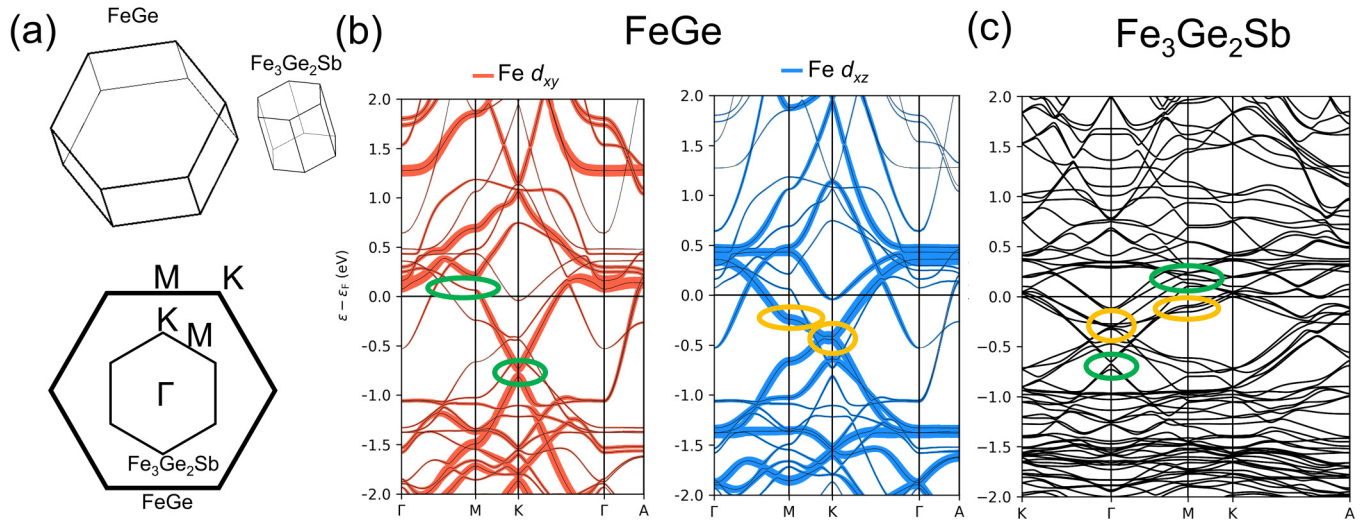


FIG. 2. (a) Comparison of the 3D and in-plane Brillouin zone of FeGe (outer) and  $\text{Fe}_3\text{Ge}_2\text{Sb}$  (inner). The  $\Gamma$  and A points are highlighted in the 3D Brillouin zone, while the in-plane points  $\Gamma$ , M and K are highlighted for the in-plane Brillouin zone. (b) Electronic structure of FeGe in the colinear antiferromagnetic state. Colored highlights indicate the location of the gapped Dirac-like state (DC 2, green) and the kagome derived Dirac state (DC 1, purple), and the two van Hove singularities (VHS 1 and 2, green and purple, respectively) (c) Electronic structure of  $\text{Fe}_3\text{Ge}_2\text{Sb}$  in the colinear antiferromagnetic state. Due to the large number of overlapping bands, the fat-band projection in  $\text{Fe}_3\text{Ge}_2\text{Sb}$  is not as clear as in FeGe and is therefore not shown. The k path is chosen to highlight the in-plane dispersion around the  $\Gamma$  point, which due to band folding, contains the features at the K point in FeGe. The same features are highlighted for FeGe are highlighted here, with VHS 1 being labeled with an asterisk to denote it is strongly split and perturbed compared to in FeGe.

assumed in the center of the kagome plane is assumed to be a 0.179(7) occupancy of Ge, the composition from single crystal x-ray diffraction becomes  $\text{Fe}_3\text{Ge}_{2.085(4)}\text{Sb}_{0.915(4)}$ , which is within error of the EDX composition; this structure is shown in Fig. 1(c). A small Sb occupancy of this site was ruled out as it leads to an unphysically large thermal parameter. This model was slightly better than that with all Sb off center and with 10% vacancy as reported in Ref. [27] and no occupancy of the site in the kagome plane. As this structure is on the end of a reported  $\text{Fe}_3\text{Ge}_{3-x}\text{Sb}_x$  solid solution, it may be that this composition and structure exists at  $x$  slightly less than, but within three standard deviations of one. This is consistent with the previous report of the composition  $\text{Fe}_3\text{Ge}_{2.35}\text{Sb}_{0.35}$ , which shows Ge for Sb disorder and Ge to retain a preference for the site within the kagome layer. Either way, some small level of disorder is expected to be associated with the Sb site in the real material. The completely ordered structure is shown in Fig. 1 for ease of comparison. The composition as determined by energy dispersive x-ray spectroscopy (EDX) is  $\text{Fe}_3\text{Ge}_{2.14(8)}\text{Sb}_{0.88(6)}$  is within three standard deviations of both the single-crystal composition and the ideal composition  $\text{Fe}_3\text{Ge}_2\text{Sb}$ , however, the single-crystal data points to the Ge for Sb disorder as shown in Fig. 1(c), which is also present in the reported  $\text{Fe}_3\text{Ge}_{3-x}\text{Sb}_x$  solid solution for  $x < 1$ .

### B. Electronic structure calculations

In order to understand how the Sb for Ge substitution and resultant dimerization and buckling modifies the electronic structure in  $\text{Fe}_3\text{Ge}_2\text{Sb}$  compared to FeGe, electronic structure calculations were performed for the colinear antiferromagnetic (AFM phase) of both FeGe and  $\text{Fe}_3\text{Ge}_2\text{Sb}$ . For FeGe,

the Fe moment in the AFM configuration was calculated to be  $1.55 \mu_B$ , in relatively good agreement with the  $1.60 \mu_B$ – $1.74 \mu_B$  range determined by neutron diffraction experiments [39]. For  $\text{Fe}_3\text{Ge}_2\text{Sb}$ , the Fe moment was calculated to be  $1.78 \mu_B$  and  $1.80 \mu_B$  on the two Fe sites. These larger values are likely due to poorer overlap between Fe and Sb than Fe and Ge due to the displacement of Sb from the layer, leading to a greater localization of charge on the magnetic Fe sublattice.

The calculated electronic structure of FeGe has been previously reported in the literature, [21,37,40,41], and our calculations are consistent with these results. The calculated electronic structure of FeGe demonstrates a few interesting features highlighted in Figs. 2(a) and 2(b). There is a gapped Dirac-like state centered around the K point at around 0.8 eV below the Fermi level, stemming primarily from Fe  $d_{xy}$  and  $d_{x^2-y^2}$  orbitals (DC 2). There is also a Dirac state derived from the kagome Fe layers that has the typical dispersion of a kagome Hamiltonian, with a crossing point at about 0.5 eV below the Fermi level at the K point, composed primarily of Fe  $d_{xz}$  and  $d_{yz}$  orbitals (DC 1). There are also van Hove singularities near the Fermi level, one slightly above (VHS 1) and one slightly below (VHS 2), consistent with angle-resolved photoemission spectroscopy (ARPES) measurements [21]. The van Hove singularity just above the Fermi level is mainly due to  $d_{x^2-y^2}$  orbitals, while the one below is mainly from  $d_{xz}$  and  $d_{yz}$ . The electronic structure of FeGe provides a possible explanation of the charge order observed in multiple kagome metal systems, which may be a generic feature of a kagome metal at certain band fillings.

The calculated electronic structure of  $\text{Fe}_3\text{Ge}_2\text{Sb}$  is shown in [Fig. 2(c)]. When comparing the electronic structure of  $\text{Fe}_3\text{Ge}_2\text{Sb}$  with that of FeGe, it is important to note that

because of the  $\sqrt{3} \times \sqrt{3} \times 2$  expansion of the unit cell and 30 degree rotation of the cell axis, band folding effects occur. By band folding, the K point of FeGe folds onto the  $\Gamma$  point of  $\text{Fe}_3\text{Ge}_2\text{Sb}$ , while the M point in FeGe remains the M point in  $\text{Fe}_3\text{Ge}_2\text{Sb}$ . While the electronic structure of  $\text{Fe}_3\text{Ge}_2\text{Sb}$  is more complex than FeGe due to a larger number of bands, we can still compare relevant features discussed above. Overall, the Fe derived states span roughly the same range of energy in FeGe and  $\text{Fe}_3\text{Ge}_2\text{Sb}$ , suggesting that the extra electron introduced by Sb is well accounted for by the formation of the Sb-Sb bond. Comparing the electronic structures shows that VHS 2 at M is preserved in  $\text{Fe}_3\text{Ge}_2\text{Sb}$  at roughly the same energy, with a weak band splitting effect Fig. 2. However, VHS 1 is strongly split in  $\text{Fe}_3\text{Ge}_2\text{Sb}$ , suggesting a possible reason for the presence of a CDW in FeGe but not in  $\text{Fe}_3\text{Ge}_2\text{Sb}$ , as this same van Hove singularity is suggested to play a role in the CDW in FeGe [22,37].

DC 1, composed of Fe  $d_{xy}$  and  $d_{x^2-y^2}$  orbitals is retained in  $\text{Fe}_3\text{Ge}_2\text{Sb}$ , projected to the  $\Gamma$  point, centered around roughly the same energy with a weak band splitting effect. DC2 also appears to be preserved in  $\text{Fe}_3\text{Ge}_2\text{Sb}$ , also projected onto the  $\Gamma$  point, with a crossing energy about 0.1 eV closer to  $E_F$  than in FeGe. This state also overlaps with a parabolic band centered around  $\Gamma$ , also present at  $\Gamma$  in FeGe, due to band folding. A new manifold of crossings is also observed at the K point in  $\text{Fe}_3\text{Ge}_2\text{Sb}$ , due to band folding effects. The retention of the Dirac states and one of the van Hove singularities, along with the selective destruction of the other van Hove singularity, suggests the possibility of tuning van Hove singularity induced CDW and superconducting states by controlling the buckling in kagome metals, with the  $\text{Fe}_3\text{Ge}_{3-x}\text{Sb}_x$  solid solution or electron doping (e.g., Te doping) in the  $\text{AV}_3\text{Sb}_5$  family representing good candidates for this chemical tuning.

### C. Magnetization and heat capacity

The temperature-dependent and isothermal magnetization of a single crystal of  $\text{Fe}_3\text{Ge}_2\text{Sb}$  were measured and shown in Fig. 3. Like FeGe,  $\text{Fe}_3\text{Ge}_2\text{Sb}$  shows two magnetic transitions, these are at 288 K and 16 K upon cooling [Fig. 3(a)], compared to 410 K and 30 K in FeGe. In FeGe these are associated with collinear antiferromagnetic order, with the Fe spins pointing along  $c$ , and a spin-canting transition to a canted antiferromagnetic state with a double spin-cone ground state [31], respectively. Due to the similarity of the shape of the magnetization versus temperature curves of FeGe and  $\text{Fe}_3\text{Ge}_2\text{Sb}$ , the 16 K transition in  $\text{Fe}_3\text{Ge}_2\text{Sb}$  is likely also a transition from a collinear antiferromagnetic state to a double spin-cone state. Neutron diffraction measurements are needed to confirm this. The similar magnetism between the two systems supports the comparison of the AFM phases when comparing the calculated electronic structures. When the field is along  $c$ , the magnetization demonstrates a small kink at the antiferromagnetic transition temperature followed by a monotonic increase of the magnetization before a sharp peak at the 16 K transition. By contrast, when the field is in plane, there is a decrease in the magnetization below the high-temperature transition at around 100 K in  $\text{Fe}_3\text{Ge}_2\text{Sb}$ . This is similar to the case of FeGe, for which the magnetization versus temperature

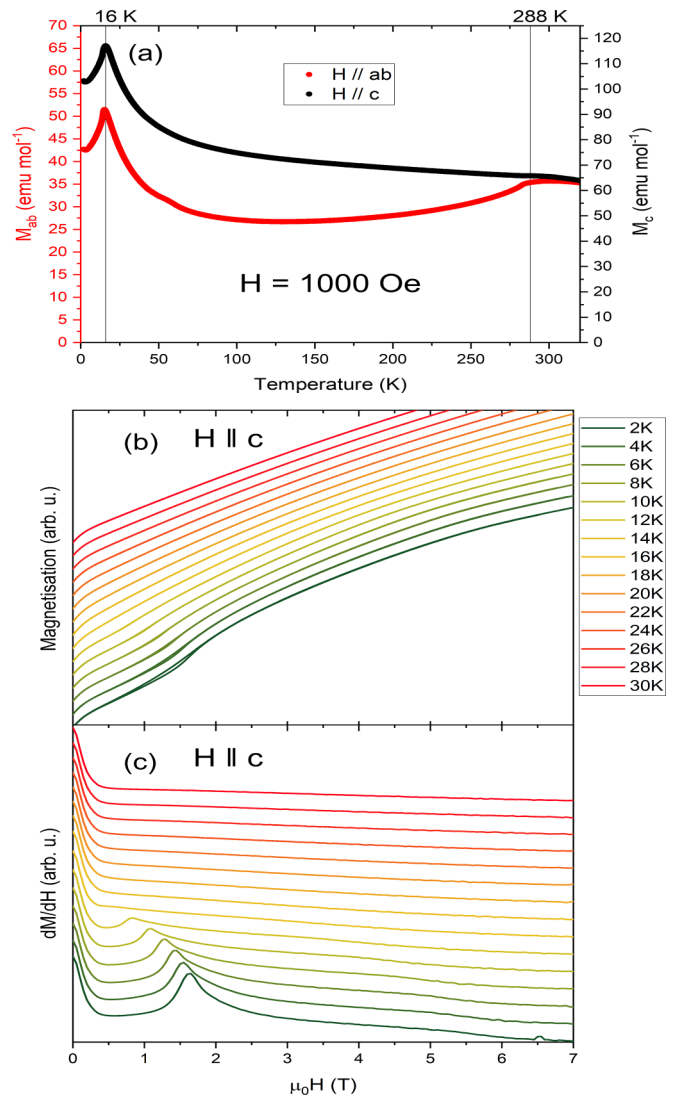


FIG. 3. (a) Magnetization versus temperature for a single crystal of  $\text{Fe}_3\text{Ge}_2\text{Sb}$ , with the field applied both along  $c$  and in the  $ab$  plane. The high-temperature antiferromagnetic and low-temperature non-collinear transition temperatures are highlighted. (b) Magnetization versus field curves near the low temperature noncollinear transition, with field along  $c$  and (c) the derivative of the magnetization versus field curves, showing a smooth variation of the metamagnetic transition on heating to 16 K, followed by its disappearance above 16 K. Both (b) and (c) are shown with offsets for better comparison of the magnetization curves at different temperatures.

has a local minimum around 60 K when the field is applied in-plane [31].

The reduction in transition temperatures upon Sb substitution implies both a reduced in-plane magnetic exchange strength and cross-plane magnetic exchange strength, likely due to the buckling of the kagome layer and the expansion of the unit cell from the larger Sb, leading to longer Fe-Fe distances. This is in contrast to FeSn, which lacks any spin-canting transition and which retains a collinear antiferromagnetic structure with the Fe moments lying in plane (as opposed to out of plane) to low temperature [42]. This implies that even despite the ideal kagome nature of the structure type,

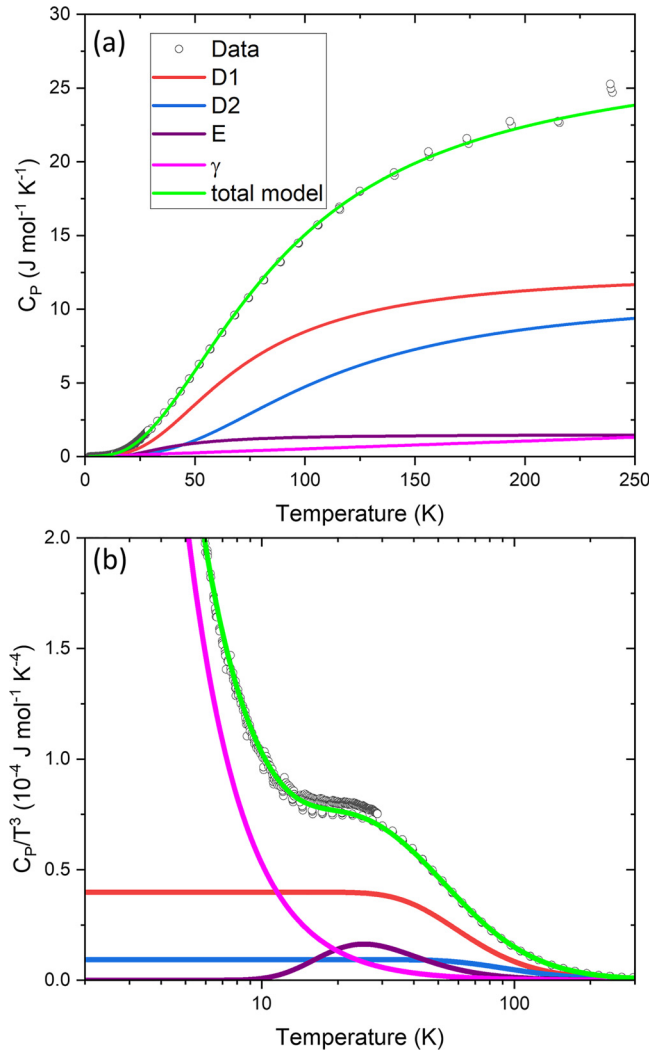


FIG. 4. Heat capacity versus temperature for  $\text{Fe}_3\text{Ge}_2\text{Sb}$  below 250 K. The fit to a phonon + electron model is shown for comparison. (b)  $C_p/T^3$  plot, with temperature on a log scale, showcasing the low temperature Einstein contribution. The data between 10 and 40 K could not be satisfactorily fit without an Einstein component.

the identity of the p-block elements that connect the kagome layers along  $c$  has a significant impact on the magnetic exchange and resulting ground state, whereas the element that occupies the kagome layer itself is less important for the magnetic structure.

The isothermal magnetizations measured between 2–30 K in applied magnetic field up to 7 T are shown in Fig. 3(b). A very small ferromagnetic component is observed, however, due to its low saturation magnetization we can attribute it to a less than 0.1% impurity, likely of  $\text{Fe}_{1.67}\text{Ge}$ . Below 16 K, the magnetization versus field curves demonstrate the appearance of a metamagnetic transition in  $\text{Fe}_3\text{Ge}_2\text{Sb}$  when the field is along the  $c$  axis. This transition occurs at a field of about 2 T at 2 K. This is analogous to the metamagnetic transition in  $\text{FeGe}$ , which occurs at 1.5 T at 2 K and is associated with a field-induced transition into another spin-cone structure, with a decreasing spin-cone half-angle as the field is increased [43]. Both spin-cone structures are reported to be long-period structures in  $\text{FeGe}$ . Figure 3(c) shows the smooth variation of

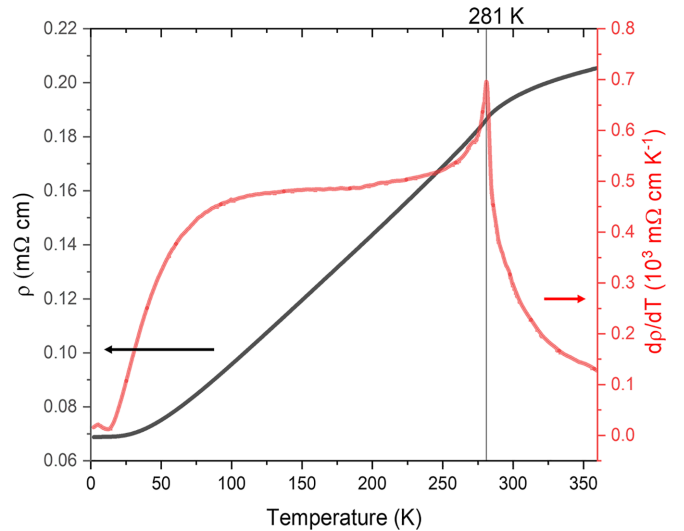


FIG. 5. Resistivity of  $\text{Fe}_3\text{Ge}_2\text{Sb}$  single crystal as a function of temperature, along with the derivative. The magnetic transition at 281 K is visible as a kink coincident with a change of curvature. The derivative shown in red shows this point clearly, as well as a broader change of slope around 16 K.

the critical field upon heating, with the transition disappearing at 16 K, confirming that the presence of the metamagnetic transition is associated with the 16 K transition.

The heat capacity as a function of temperature is shown in Fig. 4. From the temperature dependence of the heat capacity, Debye, Einstein and the electronic  $\gamma$  terms were modeled and the Debye and Einstein temperatures were extracted. Two Debye temperatures used were  $\theta_{D1} = 290$  K and  $\theta_{D2} = 450$  K along with a small Einstein contribution with  $\theta_E = 125$  K. The linear  $\gamma$  term was determined to be  $5.3 \text{ mJ mol}^{-1}\text{K}^{-2}$ , which is consistent with other Fe containing intermetallic compounds such as the value of  $5.5 \text{ mJ mol}^{-1}\text{K}^{-2}$  reported for  $\text{FeSn}$  [42] and is quite close to the free electron value of  $4.1 \text{ mJ mol}^{-1}\text{K}^{-2}$  if each Fe is considered to donate one free electron. This gives a value of  $\frac{m^*}{m_e}$  of 1.34, consistent with a relatively high effective mass from Fe 3d states. The Einstein term was needed to satisfactorily fit the data in the region 10–40 K [Fig. 4(b)], and may be associated with either the loosely held Ge or the  $\text{Sb}_2$  dumbbells. No anomalies in the heat capacity was observed at 16 K (Fig. 4), consistent with the minimal entropy associated with the transition from one fully magnetic ordered state to another, and no significant change in the nuclear positions.

#### D. Transport properties

The resistivity of a single crystal of  $\text{Fe}_3\text{Ge}_2\text{Sb}$  is shown in Fig. 5(a). A small feature is seen at the high-temperature transition, around 283 K in this sample. The resistivity has a typically metallic convex temperature dependence in the collinear antiferromagnetic state but is concave in the magnetically disordered state at higher temperatures. Below 16 K there is also a change of slope in the resistivity as is shown in the derivative, Fig. 5(b), which is compatible with a magnetic reordering. We observe no CDW transition as observed for  $\text{FeGe}$  in this temperature range.

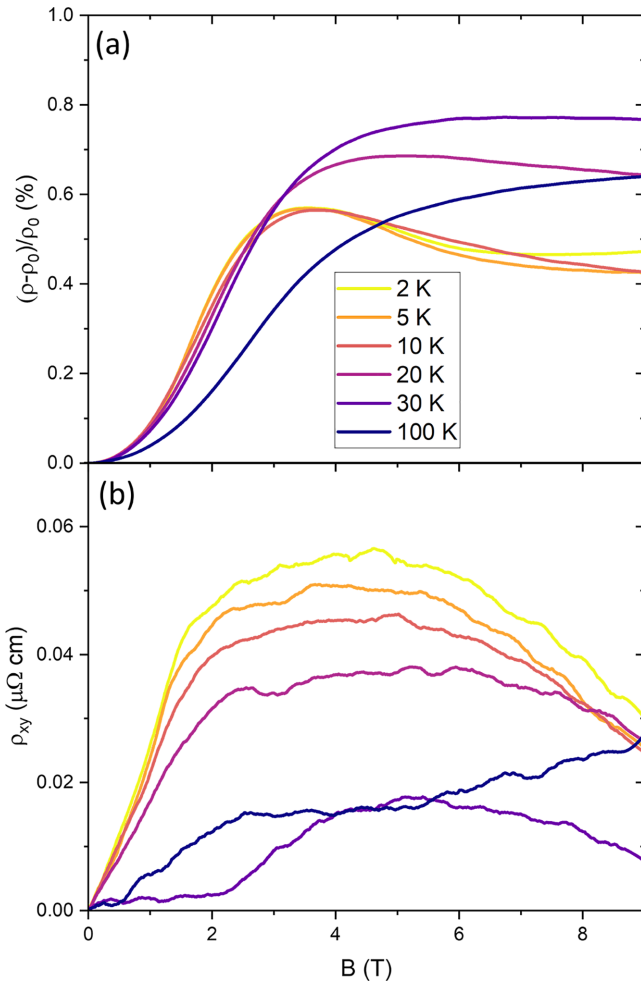


FIG. 6. (a) Transverse magnetoresistance of  $\text{Fe}_3\text{Ge}_2\text{Sb}$  single crystal in magnetic fields applied parallel to the  $c$  axis up to 9 T. At 2 K an initial positive contribution becomes negative above around 4 T before becoming slightly positive again at higher field. The negative contribution persists to at least 20 K but disappears at higher temperatures. There is no definitive signature of the metamagnetic transition seen at 2 K in the susceptibility measurements. (b) The Hall resistivity is highly non-monotonic, suggesting that multiple bands contribute to the signal. The change of slope below 2 T at 2 K may correspond to the metamagnetic transition.

The low-temperature magnetoresistance is shown in Fig. 6(a). While it is always less than 1%, it presents nonmonotonic features. After first increasing with field, it decreases again at low temperatures. While it might be tempting to identify this as the result of changes in scattering as a result of a spin reorientation transition, there is no direct correspondence to the 16 K or 2 T features seen in magnetic susceptibility. On the other hand, in FeGe there is a spin-flop transition at 7 T, which has a strong orientation dependence [31]. This suggests that the low-temperature magnetic states in  $\text{Fe}_3\text{Ge}_2\text{Sb}$  may be highly sensitive to small differences in alignment of the magnetic field with respect to the crystal axes.

In comparison, measurement of FeGe show considerably greater magnetoresistance (up to 10%) and much sharper features corresponding to the spin-flop transition observed in

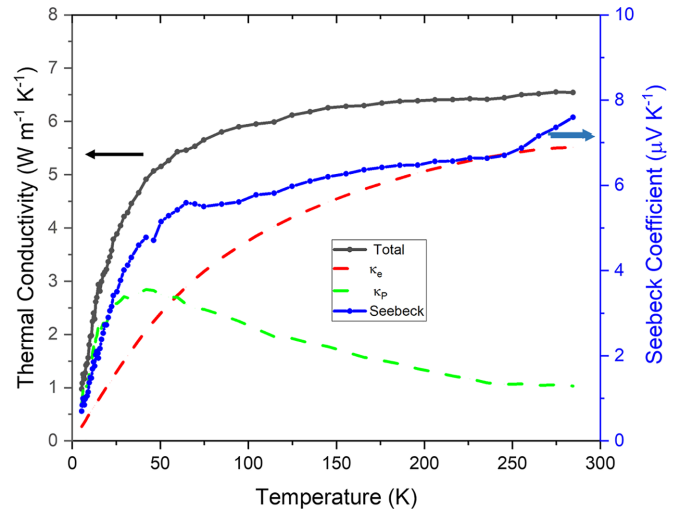


FIG. 7. Thermal conductivity and Seebeck coefficient of  $\text{Fe}_3\text{Ge}_2\text{Sb}$  as a function of temperature. The thermal conductivity is dominated by electronic carriers at high temperature (dashed curve) and by phonon transport (dotted curve) at low temperature. The Seebeck coefficient shows no remarkable temperature-dependent features.

susceptibility [44]. Those measurements were only performed with field in the basal plane, however.

On the other hand the Hall resistivity in Fig. 6(b) does feature a change in slope at around 1.8 T at temperatures below 16 K that broadens and shifts to higher fields as the temperature is increased, which is consistent with the metamagnetic transition. Unfortunately the sample is relatively resistive and the Hall signal is an order of magnitude smaller than the magnetoresistance in turn, making a positive identification difficult using this data set. On the basis of one electron per Fe, we would expect a Hall coefficient approximately ten times greater than the observed slope of  $\rho_{yx}$ , which also implies that the Hall signal is partially compensated. This is consistent with the electronic structure calculations, which show multiple bands crossing the Fermi level. While a multiband model could be used to fit the magnetoresistance and Hall data, the peak in the magnetoresistance requires more than two bands to reproduce. Given the relatively small and noisy Hall signal, the results would not be reliable.

The thermal conductivity  $\kappa$  and Seebeck coefficient  $S$  measured in zero field are shown in Fig. 7. The Wiedemann-Franz law (WFL) states that the transport of both charge and heat by the electronic carriers are subject to the same scattering processes, leading to the relation

$$L_0 = \frac{\kappa_e}{\sigma T}, \quad (2)$$

where  $L_0 = \frac{\pi^2 k_B^2}{3e^2} = 2.44 \times 10^{-8} \text{V}^2 \text{K}^{-2}$  is the Sommerfeld value of the Lorenz constant. Using this relation to estimate  $\kappa_e(T)$ , the electronic part of the thermal conductivity, implies that 80% of the heat transport at room temperature is by charge carriers (dashed curve in Fig. 7). Below 60 K other carriers of heat become dominant. The neutral thermal current,  $\kappa_p = \kappa - \kappa_e$  (dotted curve in Fig. 7), peaks around 40 K, which is of the order  $\theta_D/10$ . This is typical for heat transport

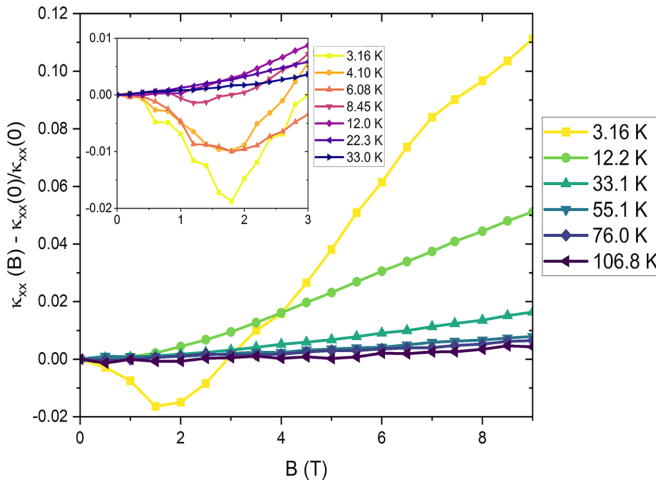


FIG. 8. (a) Magnetothermal conductivity ( $\frac{\kappa(B) - \kappa(0)}{\kappa(0)}$ ) of  $\text{Fe}_3\text{Ge}_2\text{Sb}$  as a function of magnetic field perpendicular to the kagome planes normalized to the zero field values. (b) Zoom on the low-field region with higher-resolution data. At temperatures below 10 K a negative contribution to the thermal conductivity is seen below 2 T, which is broad and disappears as the temperature is increased.

by phonons. Their relatively weak overall contribution to thermal transport may be a consequence of the buckling of the layers introduced by the presence of Sb, leading to reduced phonon velocities, as well as possible scattering from the Sb related disorder.

The Seebeck coefficient is relatively small and monotonic with temperature, showing no discernible feature at the low-temperature magnetic transition. Above 60 K it varies little with temperature. The slope of  $S(T)$  below 20 K is  $0.14 \mu\text{V K}^{-2}$ . In the low-temperature limit this slope should track any enhancement of the linear coefficient of the heat capacity above the free electron value, and indeed the ratio  $q = \frac{S}{T} \frac{N_{\text{Av}} e}{\gamma} = 2.5$  [45], which is relatively close to the expected value of  $\pm 1$ . The deviation from this value could arise from phonon drag, which may still actively contribute to the Seebeck coefficient in this temperature range.

At temperatures below 10 K, the thermal conductivity initially drops slightly as magnetic fields of up to  $\sim 2$  T are applied (Fig. 8). It then rises again at higher fields. Above 10 K this low-field feature is lost.

At 3.2 K the thermal conductivity is more than 10% higher at 9 T than in zero field. This is far in excess of the changes in magnetoresistance ( $< 1\%$  everywhere), which in any case would imply a negative contribution to the magnetothermal conductivity rather than a positive one via the WFL. We

therefore ascribe changes in the thermal conductivity to the effects on the small-angle scattering of the modification of the magnetic state as the field is applied. Small-angle scattering degrades the thermal current more efficiently than the electrical one, and is one reason why the WFL does not generally hold at intermediate temperatures [46]. It seems logical to associate this with the presence of the spin-canted state where an applied magnetic field might easily affect long-period magnetic order.

The thermal Hall effect, which should not have any contribution from phonons, should also obey the WFL and scale with the Hall conductivity. However, from the Hall data the expected maximum value is of the order  $\kappa_{yx} \lesssim 0.001 \text{ W K}^{-1} \text{ m}^{-1}$ , which is around the noise floor of our measurement, and indeed we measured no discernible  $\kappa_{yx}$ .

#### IV. CONCLUSIONS

Single crystalline  $\text{Fe}_3\text{Ge}_2\text{Sb}$  with buckled kagome Fe layers shows similar magnetic behavior to ideal kagome FeGe, with slightly modified Fe moments, transition temperatures, and metamagnetic transition fields, likely due to the difference in Fe-Fe distances and the bonding interaction between Fe and the main group metal. The metamagnetic transition shows coupling to the thermal conductivity but not the resistivity, demonstrating that it likely involves a long-period transition associated with a spin-canted ground state.  $\text{Fe}_3\text{Ge}_2\text{Sb}$  shows multicarrier behavior, and does not have the CDW transition present in FeGe. Electronic structure calculations show that only the van Hove singularity at M is affected by the buckling, a likely reason for the lack of CDW. Overall, the addition of the extra electron and formation of dimers only modestly affects the properties, demonstrating that control of the buckling in kagome metals may be a way to tune the presence or absence of van Hove singularities and CDWs without disrupting the electronic structure and magnetic behavior associated with the underlying kagome net, and that an incipient buckling instability with a corresponding dimer formation may be related to the charge order, or lack thereof, observed in other kagome metal systems.

Full data sets can be found at [47].

#### ACKNOWLEDGMENTS

The authors would like to acknowledge funding from the Engineering and Physical Sciences Research Council (EPSRC) Programme Grants (No. EP/N004884 and No. EP/V026887).

- [1] S. Yan, D. A. Huse, and S. R. White, *Science* **332**, 1173 (2011).
- [2] H. Takagi, T. Takayama, G. Jackeli, G. Khaliullin, and S. E. Nagler, *Nature Rev. Phys.* **1**, 264 (2019).
- [3] P. Khuntia, M. Velázquez, Q. Barthélemy, F. Bert, E. Kermarrec, A. Legros, B. Bernu, L. Messio, A. Zorko, and P. Mendels, *Nature Phys.* **16**, 469 (2020).
- [4] H.-M. Guo and M. Franz, *Phys. Rev. B* **80**, 113102 (2009).

- [5] I. Mazin, H. O. Jeschke, F. Lechermann, H. Lee, M. Fink, R. Thomale, and R. Valentí, *Nature Commun.* **5**, 4261 (2014).
- [6] H. Zhao, H. Li, B. R. Ortiz, S. M. Teicher, T. Park, M. Ye, Z. Wang, L. Balents, S. D. Wilson, and I. Zeljkovic, *Nature (London)* **599**, 216 (2021).
- [7] B. R. Ortiz, S. M. L. Teicher, Y. Hu, J. L. Zuo, P. M. Sarte, E. C. Schueller, A. M. Milinda Abeykoon, M. J. Krogstad, S.

- Rosenkranz, R. Osborn *et al.*, *Phys. Rev. Lett.* **125**, 247002 (2020).
- [8] Y.-X. Jiang, J.-X. Yin, M. M. Denner, N. Shumiya, B. R. Ortiz, G. Xu, Z. Guguchia, J. He, M. S. Hossain, X. Liu *et al.*, *Nature Mater.* **20**, 1353 (2021).
- [9] C. Guo, C. Putzke, S. Konyzheva, X. Huang, M. Gutierrez-Amigo, I. Errea, D. Chen, M. G. Vergniory, C. Felser, M. H. Fischer *et al.*, *Nature (London)* **611**, 461 (2022).
- [10] N. Shumiya, M. S. Hossain, J.-X. Yin, Y.-X. Jiang, B. R. Ortiz, H. Liu, Y. Shi, Q. Yin, H. Lei, S. S. Zhang *et al.*, *Phys. Rev. B* **104**, 035131 (2021).
- [11] H. Li, B. Ding, J. Chen, Z. Li, Z. Hou, E. Liu, H. Zhang, X. Xi, G. Wu, and W. Wang, *Appl. Phys. Lett.* **114**, 192408 (2019).
- [12] L. Ye, M. Kang, J. Liu, F. Von Cube, C. R. Wicker, T. Suzuki, C. Jozwiak, A. Bostwick, E. Rotenberg, D. C. Bell *et al.*, *Nature (London)* **555**, 638 (2018).
- [13] E. Liu, Y. Sun, N. Kumar, L. Muechler, A. Sun, L. Jiao, S.-Y. Yang, D. Liu, A. Liang, Q. Xu *et al.*, *Nature Phys.* **14**, 1125 (2018).
- [14] S. N. Guin, P. Vir, Y. Zhang, N. Kumar, S. J. Watzman, C. Fu, E. Liu, K. Manna, W. Schnelle, J. Gooth *et al.*, *Adv. Mater.* **31**, 1806622 (2019).
- [15] M. Kang, L. Ye, S. Fang, J.-S. You, A. Levitan, M. Han, J. I. Facio, C. Jozwiak, A. Bostwick, E. Rotenberg *et al.*, *Nature Mater.* **19**, 163 (2020).
- [16] M. Kang, S. Fang, L. Ye, H. C. Po, J. Denlinger, C. Jozwiak, A. Bostwick, E. Rotenberg, E. Kaxiras, J. G. Checkelsky, and R. Comin, *Nature Commun.* **11**, 4004 (2020).
- [17] Z. Liu, M. Li, Q. Wang, G. Wang, C. Wen, K. Jiang, X. Lu, S. Yan, Y. Huang, D. Shen *et al.*, *Nature Commun.* **11**, 4002 (2020).
- [18] W. R. Meier, M.-H. Du, S. Okamoto, N. Mohanta, A. F. May, M. A. McGuire, C. A. Bridges, G. D. Samolyuk, and B. C. Sales, *Phys. Rev. B* **102**, 075148 (2020).
- [19] M. Jovanovic and L. M. Schoop, *J. Am. Chem. Soc.* **144**, 10978 (2022).
- [20] J.-X. Yin, Y.-X. Jiang, X. Teng, M. S. Hossain, S. Mardanya, T.-R. Chang, Z. Ye, G. Xu, M. M. Denner, T. Neupert *et al.*, *Phys. Rev. Lett.* **129**, 166401 (2022).
- [21] X. Teng, L. Chen, F. Ye, E. Rosenberg, Z. Liu, J.-X. Yin, Y.-X. Jiang, J. S. Oh, M. Z. Hasan, K. J. Neubauer *et al.*, *Nature (London)* **609**, 490 (2022).
- [22] X. Teng, J. S. Oh, H. Tan, L. Chen, J. Huang, B. Gao, J.-X. Yin, J.-H. Chu, M. Hashimoto, D. Lu, C. Jozwiak *et al.*, *Nature Phys.* **19**, 814 (2023).
- [23] G. Venturini, H. Ihou-Mouko, C. Lefevre, S. Lidin, B. Malaman, T. Mazet, J. Tobola, and A. Verniere, *Chem. Met. Alloys*, **1**, 24 (2008).
- [24] J.-X. Yin, W. Ma, T. A. Cochran, X. Xu, S. S. Zhang, H.-J. Tien, N. Shumiya, G. Cheng, K. Jiang, B. Lian *et al.*, *Nature (London)* **583**, 533 (2020).
- [25] D. Chen, C. Le, C. Fu, H. Lin, W. Schnelle, Y. Sun, and C. Felser, *Phys. Rev. B* **103**, 144410 (2021).
- [26] G. Pokharel, S. M. L. Teicher, B. R. Ortiz, P. M. Sarte, G. Wu, S. Peng, J. He, R. Seshadri, and S. D. Wilson, *Phys. Rev. B* **104**, 235139 (2021).
- [27] A. M. Mills and A. Mar, *J. Alloys Compd.* **298**, 82 (2000).
- [28] O. V. Dolomanov, L. J. Bourhis, R. J. Gildea, J. A. Howard, and H. Puschmann, *J. Appl. Crystallogr.* **42**, 339 (2009).
- [29] G. M. Sheldrick, *Acta Crystallogr. A* **71**, 3 (2015).
- [30] G. M. Sheldrick, *Acta Crystallogr. C: Struct. Chem.* **71**, 3 (2015).
- [31] O. Beckman, K. Carrander, L. Lundgren, and M. Richardson, *Phys. Scr.* **6**, 151 (1972).
- [32] Q. D. Gibson, T. Zhao, L. M. Daniels, H. C. Walker, R. Daou, S. Hébert, M. Zanella, M. S. Dyer, J. B. Claridge, B. Slater *et al.*, *Science* **373**, 1017 (2021).
- [33] F. Pawula, R. Daou, S. Hébert, O. Lebedev, A. Maignan, A. Subedi, Y. Kakefuda, N. Kawamoto, T. Baba, and T. Mori, *Phys. Rev. B* **99**, 085422 (2019).
- [34] P. Blaha, K. Schwarz, F. Tran, R. Laskowski, G. Madsen, and L. Marks, *J. Chem. Phys.* **152**, 074101 (2020).
- [35] J. P. Perdew, K. Burke, and M. Ernzerhof, *Phys. Rev. Lett.* **77**, 3865 (1996).
- [36] A. M. Mills, R. Lam, and A. Mar, *Canad. J. Chem.* **76**, 1588 (1998).
- [37] H. Miao, T. Zhang, H. Li, G. Fabbris, A. Said, R. Tartaglia, T. Yilmaz, E. Vescovo, S. Murakami, L. Feng *et al.*, [arXiv:2210.06359](https://arxiv.org/abs/2210.06359).
- [38] J. Allred, S. Jia, M. Bremholm, B. Chan, and R. Cava, *J. Alloys Compd.* **539**, 137 (2012).
- [39] J. Forsyth, C. Wilkinson, and P. Gardner, *J. Phys. F: Met. Phys.* **8**, 2195 (1978).
- [40] C. Setty, C. A. Lane, L. Chen, H. Hu, J.-X. Zhu, and Q. Si, [arXiv:2203.01930](https://arxiv.org/abs/2203.01930).
- [41] S. Shao, J.-X. Yin, I. Belopolski, J.-Y. You, T. Hou, H. Chen, Y.-X. Jiang, M. S. Hossain, M. Yahyavi, C.-H. Hsu, and Y. P. Feng, *ACS nano* **17**, 10164 (2023).
- [42] B. C. Sales, J. Yan, W. R. Meier, A. D. Christianson, S. Okamoto, and M. A. McGuire, *Phys. Rev. Mater.* **3**, 114203 (2019).
- [43] J. Bernhard, B. Lebech, and O. Beckman, *J. Phys. F: Met. Phys.* **18**, 539 (1988).
- [44] B. Stenström and L. J. Sundström, *Phys. Scr.* **6**, 164 (1972).
- [45] K. Behnia, D. Jaccard, and J. Flouquet, *J. Phys.: Condens. Matter* **16**, 5187 (2004).
- [46] K. Behnia, R. Bel, Y. Kasahara, Y. Nakajima, H. Jin, H. Aubin, K. Izawa, Y. Matsuda, J. Flouquet, Y. Haga, Y. Ōnuki, and P. Lejay, *Phys. Rev. Lett.* **94**, 156405 (2005).
- [47] <https://datacat.liverpool.ac.uk/1734/>.